The Astronomical Journal, 140:1891–1904, 2010 December doi:10.1088/0004-6256/140/6/1891

SPITZER OBSERVATIONS OF A1763. II. CONSTRAINING THE NATURE OF ACTIVITY IN THE CLUSTER-FEEDING FILAMENT WITH VLA AND *XMM-NEWTON* DATA

Louise O. V. Edwards[1], Dario Fadda[1], David T. Frayer[2], Gastao B. Lima Neto[3], and Florence Durret[4]
[1] NASA Herschel Science Center, Caltech 100-22, Pasadena, CA 91125, USA; louise@ipac.caltech.edu
[2] NRAO, Green Bank, WV 24944, USA
[3] Instituto Astronomico e Geofisico, Universidade de Sao Paulo, Cidade Universitaria, BR Sao Paulo, SP 05508-900, Brazil
[4] Institut d'Astrophysique de Paris, 98 bis boulevard Arago, FR75014 Paris, France
Received 2010 January 15; accepted 2010 September 24; published 2010 November 9

ABSTRACT

The A1763 superstructure at $z = 0.23$ contains the first galaxy filament to be directly detected using mid-infrared observations. Our previous work has shown that the frequency of starbursting galaxies, as characterized by 24 μm emission is much higher within the filament than at either the center of the rich galaxy cluster, or the field surrounding the system. New Very Large Array and *XMM-Newton* data are presented here. We use the radio and X-ray data to examine the fraction and location of active galaxies, both active galactic nuclei (AGNs) and starbursts (SBs). The radio far-infrared correlation, X-ray point source location, IRAC colors, and quasar positions are all used to gain an understanding of the presence of dominant AGNs. We find very few MIPS-selected galaxies that are clearly dominated by AGN activity. Most radio-selected members within the filament are SBs. Within the supercluster, three of eight spectroscopic members detected both in the radio and in the mid-infrared are radio-bright AGNs. They are found at or near the core of A1763. The five SBs are located further along the filament. We calculate the physical properties of the known wide angle tail (WAT) source which is the brightest cluster galaxy of A1763. A second double lobe source is found along the filament well outside of the virial radius of either cluster. The velocity offset of the WAT from the X-ray centroid and the bend of the WAT in the intracluster medium are both consistent with ram pressure stripping, indicative of streaming motions along the direction of the filament. We consider this as further evidence of the cluster-feeding nature of the galaxy filament.

Key words: galaxies: clusters: individual (A1763, A1770) – radio continuum: galaxies – X-rays: galaxies: clusters

Online-only material: color figure

1. INTRODUCTION

Most of the galaxies in massive clusters have long since been thought to be old, red, and retired. But, galaxy clusters themselves are dynamic systems. Hierarchical structure formation models show these systems to be connected by large-scale filaments (Bond et al. 1996; Gonzalez & Padilla 2009) as they build up over time via mergers and interactions of smaller systems (Navarro et al. 1995; Kauffmann et al. 1999; Springel et al. 2005). Many local clusters appear dynamically relaxed with Gaussian velocity distributions (Miller et al. 2005; Finn et al. 2008), smooth X-ray temperature and luminosity profiles (Peres et al. 1998; White 2000; Vikhlinin et al. 2005), and large central galaxies at their gravitational potential well (Jones & Forman 1984; De Lucia & Blaizot 2007). On the other hand, tell-tail signs of ongoing and recent cluster activity is likewise seen: chaotic mass profiles (Zhang et al. 2009; Umetsu et al. 2010), central galaxies with wide-angle tailed (WAT) morphology (Sakelliou & Merrifield 2000; Smolčić et al. 2007), a displacement between the central galaxy and cluster mass centroid (Clowe et al. 2006; Coziol et al. 2009), and a neighboring concentration of quasars (Söchting et al. 2004) are some examples.

A1763 is one such dynamic cluster. We have gathered multi-wavelength photometry of the galaxies of this supercluster—A1763, its poorer companion A1770, and the large-scale cluster-feeding galaxy filament which connects the two. An excess of infrared (IR) bright galaxies within the filament was announced in Fadda et al. 2008 (hereafter Paper 0). Our catalog of optical, near-IR, mid-IR, and far-IR infrared photometry is presented in Edwards et al. (2010a; hereafter Paper I).

An ambiguity exists in the possible origins of the bright mid-IR detected galaxies. Most of this emission is expected to arise from current star formation, as UV light from hot stars suffers extinction through dust in the galaxy. However, emission from obscured active galactic nuclei (AGNs) can also cause significant IR radiation.

In dust obscured galaxies, the optical emission lines can lead to erroneous measurements of star formation rates (SFRs) without a solid knowledge of the extinction (Kewley & Dopita 2002). Also, optical surveys can miss up to 50% of an AGN population in luminous infrared galaxies (Imanishi et al. 2007). Similarly it has long been known that radio AGNs do not always harbor optical emission lines (Owen et al. 1995; Best et al. 2005). Fortunately, the radio emission at 1.4 GHz is well known to correlate with 24 μm and 70 μm emission from starbursts (SBs; Helou et al. 1985; Condon 1992; Yun et al. 2001). The radio emission is the synchrotron emission of relativistic electrons from past supernovae and, to some extent, free–free emission in H II regions associated with young ionizing stars. Sources with stronger radio emission relative to the FIR–radio SB correlation can be attributed to the overpowering effect of an intense AGN. This provides a method for selecting galaxies clearly dominated by radio-excess AGN. Considering that the FIR SFRs rely on the presence of dust, the radio SFRs provide a natural complement. The redder mid-IR continuum and lack of polycyclic aromatic hydrocarbon (PAH) emission in AGNs can also be pinpointed by examining the IRAC colors (Eisenhardt et al. 2004; Lacy et al. 2004).

A WAT radio galaxy lives at the center of A1763. The suggestion has been that the peculiar shape of WAT galaxies

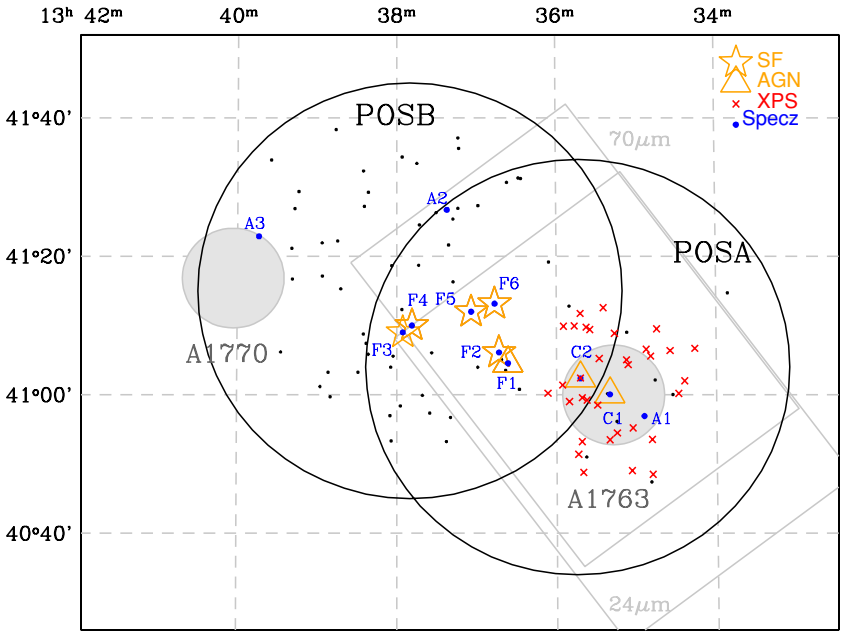

Figure 1. Coverage of photometric and spectroscopic data. Large black circles trace the FOV of the two 1.4 GHz pointings and the relative cluster positions, represented by large filled gray circles. Three σ radio detections are indicated by black dots. Those which are spectroscopically confirmed members are filled in dark blue. The eight member radio sources with MIPS 24 μm or 70 μm detections are labeled with orange. The MIPS coverage is also shown as rectangles. *XMM* observations cover the core of A1763 and X-ray point sources are marked as small red crosses. All galaxies detected in the radio and FIR lie in the cluster or toward the galaxy filament, the five furthest along the filament are star forming. Cluster core members are labeled "C", those in the filament "F" and those with absorption line spectra "A".

(A color version of this figure is available in the online journal.)

is from ram pressure caused by relative motions between the cluster gas and the plumes of the radio galaxy (Owen & Rudnick 1976). Most WATs are found to be strongly associated with optical brightest cluster galaxies (BCGs; Burns et al. 1981; Hardcastle & Sakelliou 2004), as is the case for A1763. However, strong ram pressure resulting from streaming motions of the BCG orbiting the cluster potential at high speeds seems unlikely as the galaxy should be near the bottom of the potential well of the cluster (Miley et al. 1972). Sakelliou & Merrifield (2000), Hardcastle & Sakelliou (2004) and Smolčić et al. (2007) suggest that the ram pressure resulting from the displacement of BCGs after interactions with sub-clusters is adequate in creating the WAT morphology.

Just as the small-scale structure of the WAT hints at the cluster kinematics, so does the large-scale structure. To probe this, the level of substructure and merging history of the cluster can be gleaned from the X-ray surface brightness distribution.

In this paper, we investigate the AGN and SB activity in the different environments of the superstructure and further argue for an ongoing merger and flow of filament galaxies into A1763. Observations in the radio, optical, MIR, and X-ray do not always yield the same type of AGNs (Hickox et al. 2009; Griffith & Stern 2010) and so we quantify the AGN and SB sources integrating the FIR–radio relation, X-ray point sources, and IRAC colors. We also find an overdensity of quasars near the cluster region. We separate the frequency of AGN and SB activity in the cluster versus the filament. We consider the special case of the WAT of A1763, its morphology, and location. Finally, we use unpublished archival *XMM* observations and describe the WAT and filament orientation with respect to the cluster X-ray structure. To achieve these goals, *Spitzer* photometry from Paper I is used in conjunction with new wide field 1.4 GHz Very Large Array (VLA) radio observations which cover A1763 and the filament galaxies toward A1770, and new *XMM* data which cover the cluster core.

Data and observations are discussed in Section 2, in Section 3 we show our results: an inventory of AGNs in the supercluster, radio SFRs, and a physical description of the central WAT, and the radio SFRs. In Section 4, we discuss relative contributions of AGNs and SBs, as well as the galaxy activity as a function of environment. The interplay between the large-scale (X-ray profile) and small-scale (WAT) structures leads us to conclude in Section 5 that the filament galaxies are dominated by SB systems and enhance our argument of a cluster-feeding filament. Throughout the paper, we adopt a cosmology with $\Omega_m = 0.3$, $\Omega_\lambda = 0.7$, and $H_o = 74$ km s^{-1} Mpc^{-1} where 1 arcsec = 3.5 kpc at a redshift of 0.23, unless otherwise stated.

2. OBSERVATIONS AND DATA REDUCTION

The analysis is based in part on *Spitzer* MIPS 24 μm and 70 μm observations discussed in Paper I, as well as optical spectra to be published in a forthcoming paper (D. Fadda et al. 2011, in preparation). Additionally, we provide results from new radio 1.4 GHz observations across the A1763–A1770 supercluster from the VLA and *XMM-Newton* X-ray observations of the cluster core.

2.1. VLA Observations and Reduction

We mapped the supercluster using two pointings illustrated in Figure 1 as large black circles. Cluster core members are labeled "C", those in the filament "F", and those with absorption line spectra "A". Both were made in the continuum at 1.4 GHz in 25 MHz bandwidth spectral line mode with the VLA B-configuration. A spatial resolution of 5 arcsec was achieved which is of order that of the MIPS 24 μm observations of Paper I. The observations were carried out in 30 blocks of 1.0 hr over 16 nights between March 27 and 2009 April 13 as listed in Table 1. Here we also list the primary beam at the half power point (PB). The calibrator source 1331+305 was observed at the

Table 1
Radio Observations

Pointing	R.A. (J2000)	Decl. (J2000)	*N* Blocks	IT/Block (minute)	PB (arcmin)	rms (μJy)
A1763A	13 35 45.00	+41 04 00.000	30	20.68	30	132
A1763B	13 37 50.00	+41 14 00.000	30	20.68	30	28
1331+305	13 31 08.29	+30 30 32.958	30	16.38	...	...

beginning and end of each block. It was bright, stable, and close to the target cluster so was used as both the complex gain and bandpass calibrator.

The data reduction and visualization was performed using AIPS. We followed the procedures outlined in the AIPS cookbook[5] as well as for the particular case of wide field *L*-band imaging as outlined on the NRAO Web sites[6] and in Owen & Morrison (2008). A first round of flagging was performed on the uncalibrated *u*–*v* data using UVFLAG and TVFLAG to remove dysfunctional antennas and bad time periods. The data taken on different days were immediately combined using DBCON and INDXR. Spurious *u*–*v* data points with uncalibrated fluxes greater than 6 Jy for the calibrator, and greater than 1 Jy for the sources in A1763A (the central pointing) and in A1763B (the pointing towards the filament), were also removed.

The calibrator was then SPLIT from the rest of the data and phase self-calibrated using CALIB. We used BPASS to produce the bandpass correction table which is applied directly to the other sources.

The first-pass calibration used observations of the calibrator, 1331+305. The flux of the primary calibrator was found using SETJY and VLACALIB created the SN table (the solution table stores the complex gains determined from the calibrator). We use antenna 19 for reference as it is near the center of the array and reliable during the entire observation period. VLACLCAL was then run creating the CL table to be applied to the data. This calibration table stores smoothed complex gains and corrections as a function of time to be applied to each source.

Because there are sufficiently bright sources in the pointings, self-calibration was used to refine the accuracy. Here we split the two pointings and self-calibrated each separately. Boxes were set around all real sources, and for each pointing, IMAGR and CALIB were used iteratively. First phase only calibrations are twice applied, then phase+amplitude. For A1763A, the BCG is very bright and PEELR was run to self-calibrate separately from the rest of the field. Finally, PBCOR was run on each pointing to correct for the primary beam. Reduced data from the different stokes and IFs were averaged together. An rms map for each pointing was created using the task RMSD.

2.2. XMM Observations and Reduction

The Observation Data Files (ODF ID 0084230901) of A1763 were retrieved from the *XMM-Newton* archive. We then processed them using the standard tasks *emchain* and *epchain* from the Science Analysis System (SAS) version 8.0.0. The observation was done in full window extended with the medium filter.

We produced "clean" event files by filtering out events with pattern larger than 12 in MOS and 4 in pn, and selecting only events in the FOV. The light curves in the (10–12 keV) band showed that there were high particle background time intervals during the observations. Filtering out the periods with flares reduced the exposure times from 17.4 ks to 13.6 ks (MOS) and from 11.6 ks to 9.2 ks (pn).

With the cleaned and filtered event files, we created the redistribution matrix file and ancillary response file with the SAS tasks `rmfgen` and `arfgen` for each camera and for each region analyzed.

The background was taken into account by extracting spectra from the blank sky templates described by Carter & Read (2007) and reprojected to the coordinates and roll angle of the A1763 observation. The background spectra for each detector were normalized following the procedure used in Laganá et al. (2008), by comparing each to the background extracted from the cluster observation itself, but in an annulus between 12.5 and 14 arcmin, where contribution from A1763 is not detected.

2.3. Radiometry and Catalog Matching

We used the AIPS source detection algorithm, SAD, to derive fluxes for radio sources down to the 3σ level in both fields. The BCG, an extended source, has a total flux of 350 mJy, and unfortunately lies close to the center of the A1763A pointing, limiting the dynamic range. The measured rms near the center is therefore 132 μJy (and 2×132 μJy at the half power point), whereas it is only 28 μJy (2×28 μJy at the half power point) in the center of the A1763B pointing. In order to analyze comparable detection limits between the two pointings the 3σ sources in A1763A should be compared to the 14σ sources in A1763B (a flux limit of $\sim$0.40 mJy in both cases).

SAD fails for very large and extended sources. We therefore visually examined the catalog. In cases where it was clear that a large source has been broken up into several smaller sources, we removed these false detections from the catalog and instead included the result from IMEAN, which produce the peak and integrated flux densities in a region specified with TVWIN and give similar results to those obtained from JMFIT. We provide the rms error given by IMEAN but note it is similar to the rms value from the map created with RMSD within the same area the photometry was measured in. In the few cases with a clear lobe+central source morphology, we kept the object as one detection and included the flux from the lobes as well as the central source.

To discriminate the radio sources between members and nonmembers of the superstructure, we matched the $\sim$614 3σ radio detections to optical and redshift catalogs. The Sloan Digital Sky Survey, DR7 (hereafter SDSS) covers the entire field in the u', g', r', i', and z' bands. In this paper, the optical colors, all photometric redshifts, and many spectroscopic redshifts are collected from the SDSS. In addition, we have obtained many spectra from runs with the Hydra instrument on WIYN and from TNG (D. Fadda et al. 2011, in preparation). We use the reliability method of Ciliegi et al. (2003) and Sutherland & Saunders (1992) to compute the most probable optical association for the radio observation. This method takes into account not only the distance from both detections, but also the probability of matching to a background object by computing the overdensity of optical sources as a function of magnitude. We compute

[5] http://www.aips.nrao.edu/CookHTML/CookBook.html
[6] http://www.vla.nrao.edu/astro/guides/lowfreq/analysis/

Table 2
Radio Fluxes for Cluster Members

R.A. (J2000) (deg)	Decl. (J2000) (deg)	Peak Flux (mJy beam^{-1})	Total Flux (mJy)	Pointing	Photo z	Spec z	q_{24}	q_{70}	Label
203.729874	40.607719	49.34 ± 3.43	130.54 ± 12.01	A1763A	0.2560	...	−1.90	...	
204.127914	40.944340	23.78 ± 0.13	26.04 ± 0.24	A1763A	0.2472	...	−2.07	...	
203.722885	40.945854	18.29 ± 0.31	68.59 ± 1.42	A1763A	0.1930	...	−1.47	...	
203.833618	41.001053	205.10 ± 0.13	349.90 ± 0.32	A1763A	0.2334	0.2280	−3.24	...	C1
204.321533	41.034107	0.18 ± 0.06	1.23 ± 0.43	A1763B	0.2669	...	0.55	1.59	
203.925201	41.039402	0.92 ± 0.28	0.98 ± 0.51	A1763A	0.1806	0.2181	0.23	...	C2
204.152267	41.076385	2.07 ± 0.03	6.03 ± 0.10	A1763A	0.1949	0.2345	−0.18	0.57	F1
204.364975	41.082771	0.07 ± 0.05	0.21 ± 0.19	A1763B	0.2311	...	0.72	...	
204.179306	41.101704	0.22 ± 0.03	0.19 ± 0.04	A1763A	0.1563	0.2316	1.73	2.40	F2
204.480927	41.150002	0.29 ± 0.05	0.28 ± 0.08	A1763B	0.1866	0.2311	1.17	...	F3
204.452316	41.166481	0.42 ± 0.04	0.37 ± 0.07	A1763B	0.2277	0.2564	0.66	1.82	F4
204.265793	41.199951	0.28 ± 0.05	1.41 ± 0.30	A1763B	0.2529	0.2576	0.81	2.14	F5
204.194122	41.219238	0.22 ± 0.06	0.66 ± 0.24	A1763B	0.1229	0.2330	0.57	2.07	F6
204.547623	41.312935	1.02 ± 0.04	1.13 ± 0.09	A1763B	0.1999	...	...	1.22	
204.475113	41.288013	0.09 ± 0.04	0.07 ± 0.06	A1763B	0.2031	...	...	2.09	
203.726074	40.948601	2.05 ± 0.34	1.71 ± 0.52	A1763A	0.2458	0.2380	...	...	A1
203.841034	41.002407	7.84 ± 0.37	10.19 ± 0.76	A1763A	0.2604	...	...	...	
204.304626	41.592812	1.55 ± 0.25	10.39 ± 1.90	A1763B	0.2391	...	...	...	
204.342300	41.444931	1.35 ± 0.11	3.18 ± 0.36	A1763B	0.2263	0.2564	...	...	A2
204.690735	41.638103	1.80 ± 0.32	22.38 ± 4.30	A1763B	0.1817	...	...	...	
204.932495	41.381260	1.12 ± 0.03	2.39 ± 0.08	A1763B	0.2700	0.2535	...	...	A3
204.515198	41.310566	0.46 ± 0.04	0.46 ± 0.08	A1763B	0.1839	...	...	...	
204.675247	41.254757	0.22 ± 0.04	0.63 ± 0.17	A1763B	0.2667	...	...	...	
204.491089	41.281853	0.12 ± 0.04	0.42 ± 0.16	A1763B	0.2200	...	...	...	
204.549469	41.160805	0.11 ± 0.04	0.79 ± 0.36	A1763B	0.2660	...	...	...	
204.613235	41.226471	0.11 ± 0.04	0.44 ± 0.20	A1763B	0.2257	...	...	...	
204.638367	41.196552	0.15 ± 0.04	0.23 ± 0.10	A1763B	0.2259	...	...	...	
204.685532	41.100777	0.18 ± 0.05	0.91 ± 0.30	A1763B	0.1994	...	...	...	
204.780914	41.262924	0.17 ± 0.06	0.70 ± 0.32	A1763B	0.2745	...	...	...	

reliabilities from all possible optical associations <3.5 arcsec of the radio detection in magnitude bins of 0.5 from $r' =$ 15–25. There are 135 matches, 117 of which have very good reliabilities of >0.90. All have a reliability >0.44. Of the 135 radio sources that have optical associations, 30 have spectra (with 13 confirmed cluster members) and an additional 21 have photometric redshifts between 0.18 and 0.28. Certainly some of the photometric members are real, but for this analysis we will focus only on the spectroscopically confirmed cluster members.

Table 2 shows the radio flux densities for possible cluster members with those that have confirmed redshifts labeled. The first two columns give the right ascension and declination. Columns 3 and 4 list the peak flux per beam and total flux for the 5σ detections (we include the additional 3σ sources in A1763B). The errors quoted with the fluxes are computed assuming the central rms value for photometry done with SAD. For the sources whose photometry was measured using IMEAN, we measured the local rms value. The 5σ error for pointing A1763A is 0.5 mJy and 0.2 mJy for pointing A1763B, which does not include the absolute flux calibration error of ∼15%. The total flux is always less than the peak flux, within the stated errors. The next column gives the pointing. The error on the VLA positions is ∼0.6 FWHM/(S/N) (Condon 1997), which is typically ∼1 arcsec for our data. We include only the 28 matches which have counterparts closer than 3.0 arcsec. The photometric and spectroscopic redshifts are listed in the next two columns. The values for q_{24} and q_{70} are included where available for the spectroscopic sources, and the galaxy label is included in the last column.

The ∼1° region around A1763 which covers most of A1763A and approximately half the length of the filament has been observed with *Spitzer*. MIPS 24 μm counterparts to the radio sources were found by using the same reliability method we used to choose the SDSS counterparts. The MIPS 70 μm counterpart is taken to be that closest to the radio source and must be within 10 arcsec.

Figure 2 shows a histogram of radio-detected source fluxes from both the A1763A and A1763B fields. The top plot shows 614 3σ radio sources in the region, 135 have SDSS detections, and 30 have spectroscopic counterparts. Thirteen of the radio-selected sources have spectroscopic redshifts between 0.21 and 0.26 (the redshift of A1763 is 0.23). Most radio sources have flux densities between 500 and 1000 μJy and the distribution of spectroscopic members is the same as for the entire population. The histogram on the bottom shows that 76 have MIPS 24 μm or 70 μm counterparts. The distribution of radio fluxes for the MIPS sub-samples echoes that of the full sample.

2.3.1. Detection Limits

For the radio sources with spectra, we can calculate the limiting radio luminosity at 1.4 GHz. The top panel of Figure 3 shows the histogram of radio luminosities for galaxies at the redshift of the cluster. The bottom panel shows the optical colors for all galaxies (members and non-members) located in the region observed by both MIPS and the VLA. At the mean redshift of the cluster, $z = 0.23$, the distance is 1085 Mpc. The limiting 3σ 1.4 GHz flux density of 0.4 mJy in A1763A leads to $\log L_{1.4\,\mathrm{GHz}} = 22.75$, $\log L_{1.4\,\mathrm{GHz}} = 22.08$ for A1763B. Note that the distribution of colors is similar for the population of MIPS galaxies as a whole (white histograms), as for the subset of

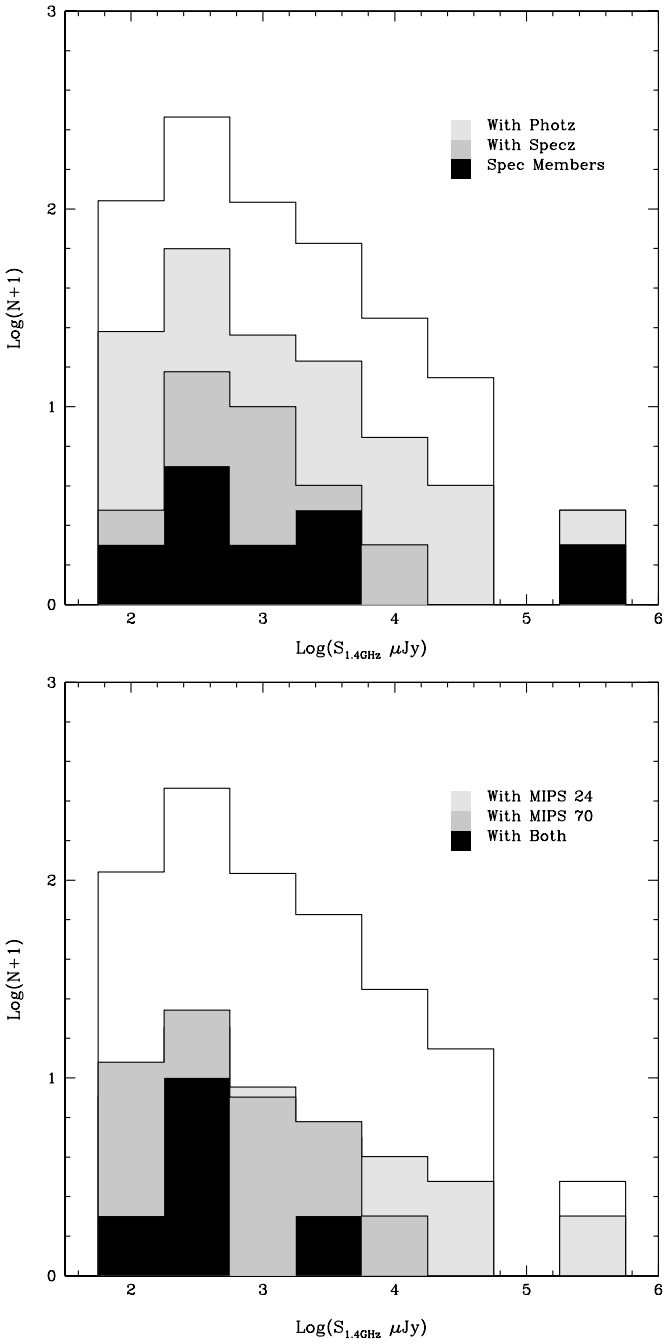

Figure 2. Histograms of the radio source flux density. Top: galaxies with photometric redshifts are in light gray, with spectroscopic redshifts are in dark gray, and spectroscopically confirmed supercluster members are in black. Most radio sources do not have bright optical counterparts and hence the number of redshifts is limited. Bottom: light gray represents galaxies with 24 μm detections, dark gray represents those with 70 μm detections, and black those with detections at both wavelengths. The shape of the distribution for the full sample is echoed in the FIR-detected subsamples.

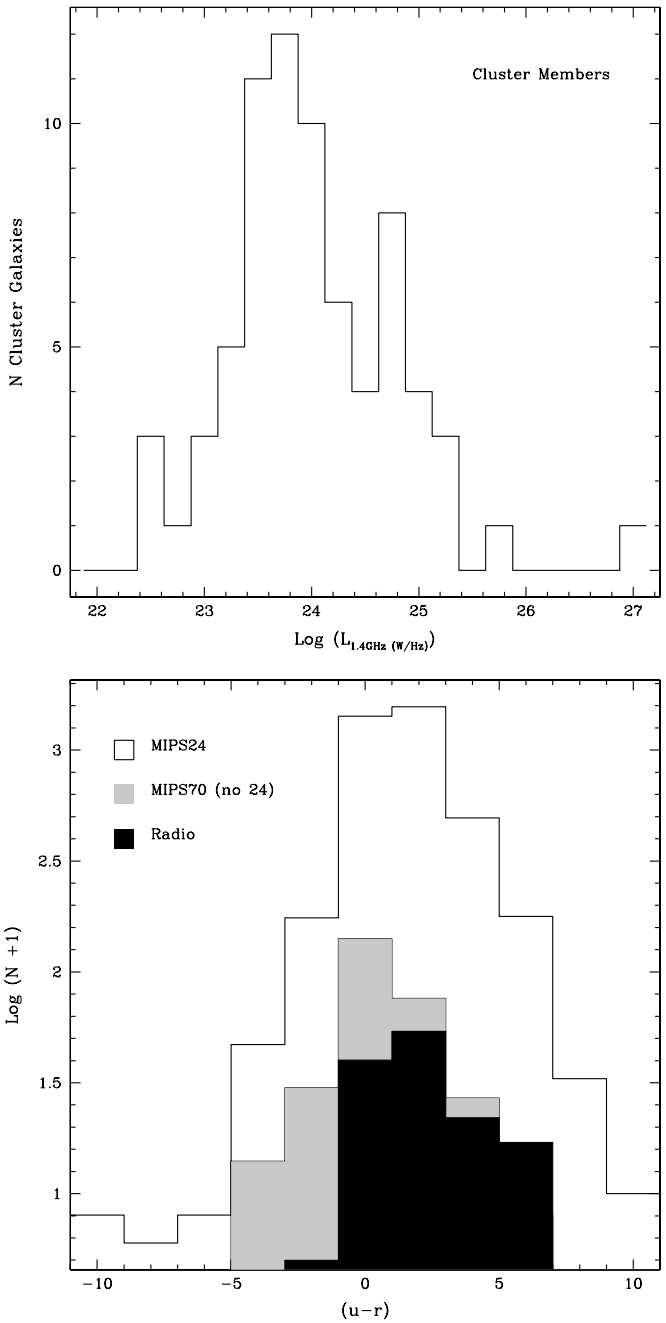

Figure 3. Histograms of the radio source luminosity and of optical colors. Top: a histogram of the radio source luminosity for only the galaxies in the cluster, where galaxies have photometric redshifts between 0.18 and 0.28 or spectroscopic redshifts between 0.21 and 0.26. Bottom: the white histogram shows the optical colors of all MIPS 24 detections (members and non-members) which also have SDSS counterparts. The gray histogram plots the colors of those with MIPS 70 detections, and the black histogram shows colors for the galaxies with radio detections as well. The radio galaxies display a range of radio intensity and those MIPS sources with radio and optical counterparts show the same distribution of optical colors.

radio-detected galaxies (black histograms). However, the radio sample does miss the bluest galaxies.

Within our detection limits, we are sensitive to all the radio-loud and most radio-excess galaxies. Yun et al. (2001) define radio-loud galaxies as those with 1.4 GHz luminosities greater than $\sim 10^{25}$ W Hz^{-1}. We find two of these in the velocity range of the cluster. Radio excess, on the other hand, is defined as having radio emission five times more than expected from the radio–FIR correlation ($q_{24} < 0.3$, where q_{24} is defined as $\log(S_{24\,\mu\mathrm{m}}/S_{1.4\,\mathrm{GHz}})$). The MIPS 24 μm 3σ limiting flux corresponds to a minimum radio flux of 40 μJy for radio-excess AGNs.

2.4. X-ray Analysis

Fitting a one-component MEKAL model to the *XMM* data using XSPEC version 11.3.2, the mean emission weighted temperature, and metallicity for the intracluster gas was obtained

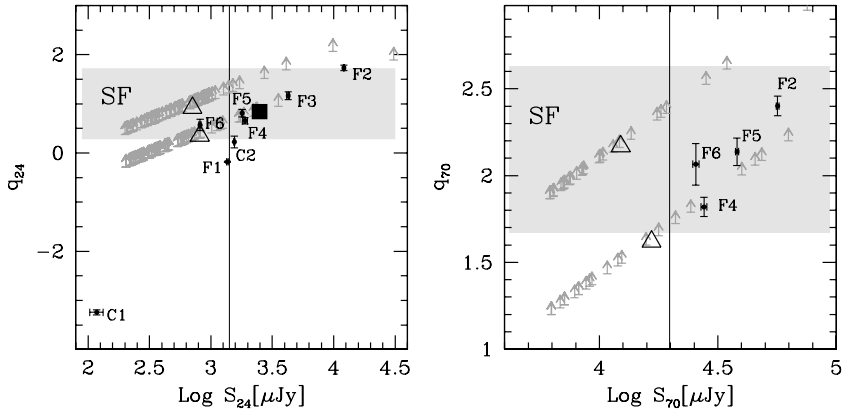

Figure 4. Radio–FIR correlation. The plots show the logarithm of the observed flux density ratio (q) vs. the infrared flux density for all spectroscopically confirmed cluster sources with an MIPS detection. Sources with MIPS 24 μm emission to the left, and with MIPS 70 μm emission are to the right. Sources with non-detections in the radio are marked as gray upper limits, with the average value shown as large open triangles. The solid gray bar indicates the best-fit radio–FIR correlation and its 3σ error, $q_{24} \sim 1 \pm 0.72$ and $q_{70} \sim 2.15 \pm 0.48$. The detection limit of position A1763A is marked as a vertical black line. The region under the correlation band is expected to be populated only by radio-excess AGN. The black square marks the q-value for the MIPS-faint stack discussed in Section 4.1.1.

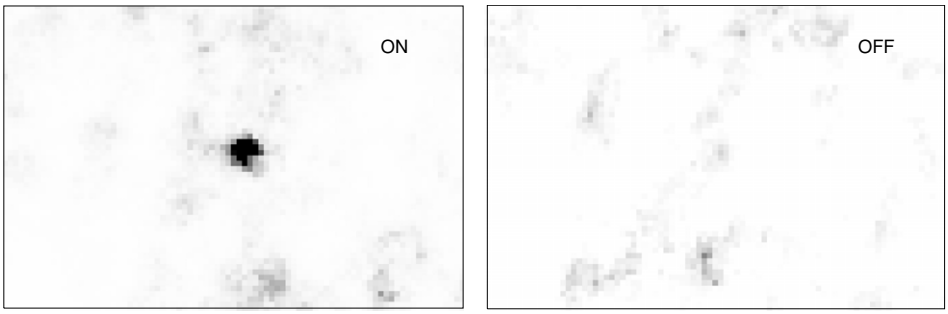

Figure 5. Faint MIPS 24 μm radio stack. A stacking analysis of the faint sources confirms that the average population of faint MIPS galaxies is consistent with SB activity. The area shown is ~2.8 arcmin across. On the right is a stack of off-MIPS positions.

inside a circle of 3.5 arcmin radius (735 kpc). With the hydrogen column density fixed at the Galactic value 0.82×10^{20} cm^{-2} (using the *nh* tool from *ftools*, based on the Leiden/Argentine/Bonn Survey) we obtained the temperature $kT = 6.8 \pm 0.3$ keV and metallicity $Z = 0.29 \pm 0.06 Z_{\odot}$ (both values at 90% confidence level).

Inside the 3.5 arcmin radius, the unabsorbed X-ray flux in the (0.5–10.0 keV) band is $f_X = (7.8 \pm 0.3)^{-12}$ erg s^{-1} cm^{-2}. The corresponding luminosity is $L_X = (1.2 \pm 0.1) \times 10^{45}$ erg s^{-1}. The unabsorbed bolometric X-ray luminosity (assuming an interval 0.01–100.0 keV) is $L_{X,\mathrm{bol}} = (1.7 \pm 0.1) \times 10^{45}$ erg s^{-1}.

3. RESULTS

Here we report three main results. We show that the AGN count is low, calculate the radio SFRs for the probable SBs, and derive the WAT properties.

3.1. Most FIR Sources are Starbursts

To help distinguish likely AGNs from SBs for the cluster and filament MIPS and radio-selected galaxies, we use various complementary methods. We check the radio–FIR correlation, find X-ray point sources, compare IRAC colors, and finally cross-correlate the positions with those of known quasars.

3.1.1. The Radio–FIR Correlation

To determine the presence of radio-excess AGNs we show the radio–FIR correlation for star-forming galaxies (Condon 1992) in Figure 4. Sources well below the relation, with a radio excess, are usually attributed to AGN emission. From Appleton et al. (2004), $q_{24} \sim 1 \pm 0.24$ and $q_{70} = \log (S_{70\,\mu\mathrm{m}}/S_{1.4\,\mathrm{GHz}}) \sim 2.15 \pm 0.16$. In our figure and analysis, we consider the 3σ error on the q-value instead of the 1σ levels published in Appleton et al. (2004). A note of caution: we are limited by the 3σ radio detection limits as the MIPS data are deeper than the radio data.

Most of the MIPS sources from Paper I are not detected in the radio and we have upper limits for most of these sources. They correspond to lower limits on the q-values of Figure 4. All cluster galaxies falling in the deeper radio pointing are classified as SB. Unfortunately, the faint MIPS end in pointing A1763A cannot all be confirmed SB from their upper limits. We calculate the average values for the upper limits in both pointings to find that both are indeed within the SB portion of the diagnostic (open triangle of Figure 4). We measure the q_{24} value for eight radio-bright member galaxies. Five are classified as SB galaxies, all along the filament are shown in Figure 1. F1 is an AGN within the filament and C1 and C2 are AGNs inside the core of A1763. All of the galaxies classified as SB through q_{24} are likewise classified as SB through q_{70}.

For the MIPS sources that are so faint that AGN and SB radio emission would both be below our radio detection limit (MIPS 24 μm flux < 400 μJy), we performed a stacking analysis. We perform this for the A1763B field since it has a deeper signal. There are 626 faint MIPS sources with high signal-to-noise ratios (S/Ns > 10) and MIPS < 4 mJy, and the median MIPS flux is 2.5 mJy. We create individual postage stamps in the radio surrounding the central pixel of the MIPS source which we then smooth by the point-source function of the MIPS data. The postage stamps are median combined together and a faint signal is detected as shown in Figure 5. The average radio flux

Table 3
XMM Point Sources in the Core of A1763

R.A. (J2000) (deg)	Decl. (J2000) (deg)	Flux (10^{-14} erg s^{-1} cm^{-2})	HR	indxPL	errIndxPL	Notes
203.781342	41.083797	20.0	−0.38	2.94	0.13	24 μm
203.924561	41.039997	10.0	0.76	0.94	0.10	24 μm 1.4GHz, C2
203.811462	40.907810	7.3	0.39	1.73	0.16	
203.834412	40.891369	5.6	0.38	1.76	0.19	
203.872421	40.974945	5.0	0.55	1.46	0.18	24 μm
203.960388	40.983299	3.9	0.59	1.36	0.20	24 μm
203.701523	40.892181	3.8	0.01	2.32	0.26	
203.853317	41.209587	3.7	0.76	0.95	0.17	24 μm 1.4GHz
203.919540	40.992699	3.6	0.61	1.33	0.20	
203.977859	41.164612	3.5	0.70	1.10	0.19	24 μm
203.762054	40.920235	3.2	0.49	1.55	0.23	
203.866241	41.086914	3.2	0.52	1.50	0.23	
203.643890	41.106319	2.8	0.47	1.60	0.25	24 μm
203.719391	41.109531	2.8	0.67	1.18	0.22	
203.895355	41.156796	2.6	0.39	1.74	0.27	24 μm
203.598740	41.033463	2.5	0.88	0.42	0.14	
204.026993	41.003651	2.4	0.23	1.99	0.30	
203.917191	40.813114	2.3	0.50	1.55	0.27	
203.924774	41.195778	2.0	0.76	0.95	0.23	
203.980515	41.023273	2.0	0.63	1.27	0.26	
203.905045	40.986900	2.0	0.59	1.37	0.28	
203.944214	41.165539	2.0	0.57	1.40	0.28	
203.764511	40.817234	1.9	0.33	1.84	0.33	
203.921417	40.887112	1.9	0.49	1.56	0.30	
203.567184	41.111725	1.8	0.48	1.58	0.32	24 μm
203.705261	41.093075	1.7	0.61	1.33	0.29	
203.906876	41.162567	1.7	0.72	1.04	0.26	
203.931854	40.856575	1.5	0.57	1.41	0.32	
203.776382	41.072380	1.5	0.79	0.84	0.25	
203.617737	41.003082	1.3	0.59	1.37	0.34	
203.818329	41.147701	1.1	−0.45	3.09	0.55	
203.701401	40.808292	1.1	0.80	0.79	0.28	
203.686234	41.158386	1.0	0.18	2.06	0.47	

is 36 μJy with an rms of 2.5 μJy (over 1000 pixels). Therefore, the q_{24}∼0.84 ± 0.04, is well within the radio–FIR correlation as shown in Figure 4 as the filled square. Therefore at least the average q_{24} for the faint MIPS population is consistent with a population of star-forming galaxies. Only 142 of the above are confirmed cluster members (we lower our allowed S/N to >3). Repeating the same analysis, the radio flux is smaller with only 19 μJy (rms = 4.6 μJy over 1320 pixels) and q_{24} is even higher at 1.26 (−1.14 +1.36).

3.1.2. X-ray Point Sources

We have selected all *XMM* point sources that have more than 25 raw counts in the 0.5–8.0 keV band in the *XMM*-pn observation, corresponding approximately to 10^{-14} erg s^{-1} cm^{-2}, for this observation. To ensure the AGN nature of the *XMM* point sources, we estimate the hardness ratio, defined as

$$\mathrm{HR} = \frac{\mathrm{hard} - \mathrm{soft}}{\mathrm{hard} + \mathrm{soft}},$$

where "soft" is the soft band 0.5–1.5 keV and "hard" is the hard band 1.5–8.0 keV. With the hardness ratio, we used *xspec* to estimate the spectrum slope, assuming the point source emission could be described by a power-law spectrum with only the Galactic absorption (i.e., no in situ absorption).

The above procedure revealed that the brightest point source in the A1763 field is probably either a nearby Young Star Object or an evolved giant red star (as seen by a bright optical counterpart on SDSS). In both cases, the X-ray emission, which is very soft, is due to wind collision. There is another source with very soft emission without an obvious optical counterpart in SDSS. The other point sources are all probably bona fide AGNs, given their slope around 1.8. The point sources that are projected onto the cluster core are listed in Table 3. If the point sources have detections either at 24 μm or 1.4 GHz, this is noted in the table.

There are other *XMM* point sources, for which we do not have spectra that may, or may not be part of the superstructure. However, only one additional source has an MIPS detection, therefore it will not affect our statistics.

The point sources with measured redshifts within the superstructure velocity include only one radio detected source, at position C2 of Figure 1. We note that there is also one bright *ROSAT* point source outside our *XMM* field of view and along the filament, at position F3 of Figure 1.

3.1.3. AGNs from the IRAC–IRAC Colors

IRAC colors can be used as diagnostics to separate stars, galaxies, and broad line AGNs (Eisenhardt et al. 2004; Lacy et al. 2004; Sajina et al. 2005; Donley et al. 2008). AGNs are well separated because the power-law AGN emission is much redder than the galaxy spectrum in the first filter, and the lack of PAHs in AGN differentiates them from the galaxies in the second filter. Lacy et al. (2004) plot 8.0/4.5 versus 5.8/3.6 which

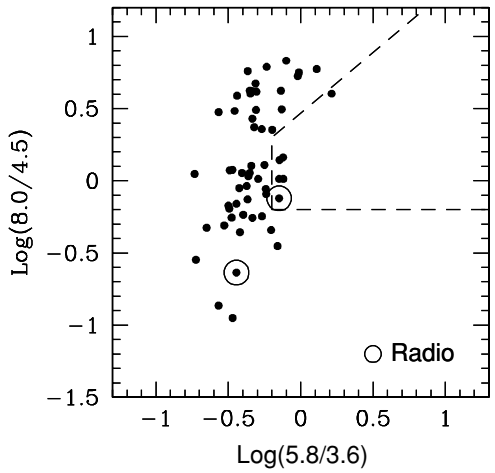

Figure 6. IRAC colors. Diagnostic diagram of Lacy et al. (2004) for the MIPS-selected galaxies which have detections in all four IRAC bands. Filled black circles are spectroscopic members. Very few of the spectroscopically confirmed members are inside of the dashed polygon, the AGN region of the diagnostic. The two galaxies in the sample with radio detections are F1 and C1.

Table 4
AGN Candidates from IRAC Colors

MIPS ID	R.A. (J2000) (deg)	Decl. (J2000) (deg)	log(*I*4/*I*2)	log(*I*3/*I*1)	*z*	Notes
4027	203.787811	40.988712	0.2142	0.6035	0.2369	
4481	203.981293	41.024662	−0.1219	0.1628	0.2351	
5035	204.152267	41.076385	−0.1493	0.01325	0.2345	
5107	204.037750	41.085625	−0.1472	0.143	0.2374	
5188	203.938751	41.089951	−0.1200	0.0128	0.2378	
4188	203.833618	41.001053	−0.6362	−0.4442	0.2280	C1
5035	204.152267	41.076385	−0.1211	−0.1493	0.2345	F1

Note. [a] Errors on the IRAC magnitudes are typically at the 10% level.

separates very well the objects with blue continua from objects with red continua, a good diagnostic of an AGN is if red colors are seen in both IRAC filters.

We plot the IRAC colors of our MIPS-selected galaxies from Paper I in Figure 6. Very few of the spectroscopically confirmed members fall into the AGN region of the Lacy et al. (2004) diagnostic diagram. This is consistent with the model results of Sajina et al. (2005) and template results of Donley et al. (2008) which both find that for low-z galaxies, the Lacy et al. (2004) diagnostic plot does a good job of separating AGN from the SB sample. Of our five galaxies that fall into the AGN region of the Lacy et al. (2004) diagnostic (Table 4), only one source, the radio-excess AGN F1 of Figure 1, is also a radio source.

3.1.4. Quasars at the Outskirts of the Superstructure

At low redshifts, $z < 0.3$, radio-quiet quasars are known to trace the large-scale structure of the universe (Söchting et al. 2004). They are usually found at the outskirts of regions of high galaxy density, like rich clusters. We therefore cross-identify the quasar catalog of Véron-Cetty & Véron (2006) to search for such objects in and around the A1763 supercluster.

There are 85 quasars in the smaller region of 13h30m $< \alpha <$ 13h44m, and 40d40m $< \delta <$ 42d20m, 11 of these have redshifts between 0.15 and 0.25. These quasars are listed in Table 5 and shown in Figure 7. The quasars which are spectroscopic cluster members are low luminosity quasars, having absolute V magnitudes that range between −20.2 and −22.7.

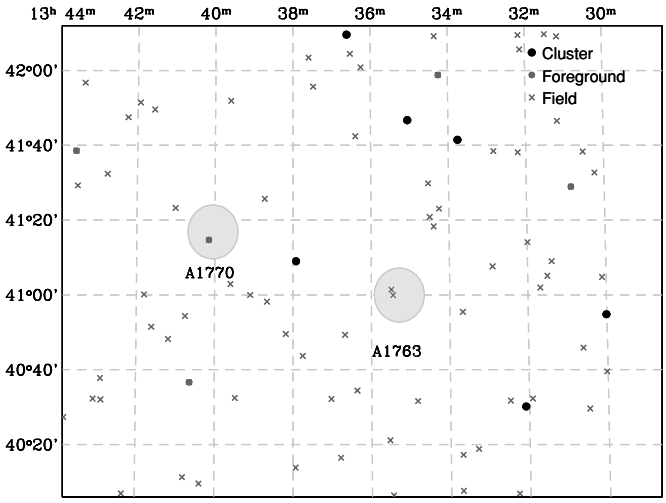

Figure 7. Quasars near the A1763 field. The positions of quasars on the sky. The gray dots refer to those quasars with $0.15<z<0.2$, and the black dots represent those with $0.2<z<0.25$. Quasars outside of these redshift windows are shown with x's. The positions of A1770 and A1763 are shown as gray circles.

Table 5
Quasar Candidates from Véron-Cetty & Véron (2006)

ID	R.A. (J2000) (deg)	Decl. (J2000) (deg)	*z*	m_V	Note
1014	202.502917	40.913891	0.248	18.95	
1031	202.713750	41.482224	0.182	17.63	
1068	203.022923	40.502777	0.240	19.41	
1119	203.439586	41.690834	0.225	18.14	
1137	203.562082	41.980000	0.168	19.50	
1173	203.762495	41.778332	0.225	19.96	
1227	204.152922	42.159447	0.224	17.40	
1259[a]	204.480835	41.150002	0.231	18.76	F3
1306[b]	205.039171	41.244999	0.167	18.62	
1322	205.159171	40.610832	0.161	17.25	
1408	205.894993	41.642502	0.164	18.56	

Notes.
[a] This galaxy is labeled as F3 elsewhere in text.
[b] Located on the outer side of A1770.

All quasars avoid the inner virial radius of the clusters with quasar ID 1322 found on the outer edge of A1770, and ID 1259 in the middle of the galaxy filament. The latter is the *ROSAT* point source F3, positioned along the filament in Figure 1.

3.2. Starburst Candidates and Radio SFRs

The previous section has shown us that most of the supercluster members are SB but that a few AGNs exist. In this section, we use the optical emission lines to look into the AGN/SB nature of the members as well as quantify the amount of star formation and compare this to the amounts calculated from the FIR and radio emission.

3.2.1. Candidates

A map of the galaxies which are spectroscopically confirmed cluster members for which we can measure q_{24} is shown in Figure 1. For the few cluster members with high radio flux densities, the SB still dominate, but the fraction of AGNs present is much higher. All radio-bright SBs and AGNs are all projected along or toward the filament. The SBs are all further from the center of A1763, and two of three of the AGNs are inside the cluster core.

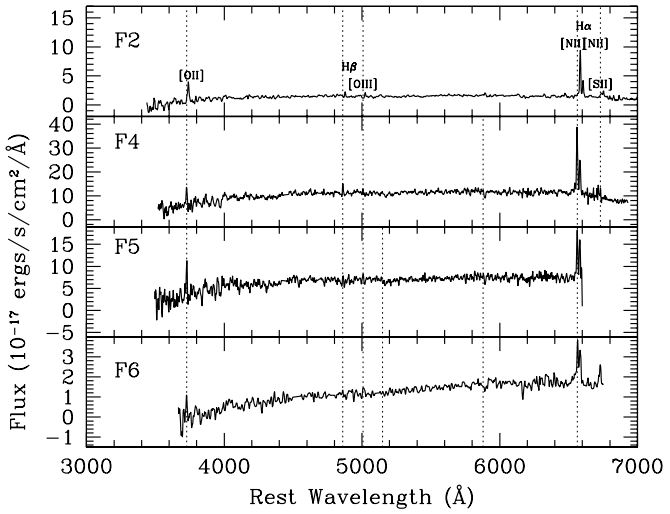

Figure 8. SB Galaxy spectra. F2, F4, F5, and F6 (as in Figure 1) all have strong Hα emission.

3.2.2. Optical Emission Lines

Figure 8 shows optical spectra of the four which have high Hα to [N II] ratios, as expected for SB or composite galaxies. Figure 9 shows the three optical spectra indicative of AGNs, as well as the optical spectra for the bright radio AGN central WAT. F3 has fairly high Hα to NII, however the lines are broad indicative of a type 1 AGN, it was also the *ROSAT* X-ray source. These spectra have been processed with in-house IDL scripts that correct for the bias, cosmic rays, flat fielding, perform wavelength calibration, sky subtraction, atmospheric extinction, and correct for internal galactic extinction. The details of the data reduction process can be found in Marleau et al. (2007). We measured emission lines by minimizing the chi square fit of multiple Gaussians (for deblending emissions and any absorption) and a line for the continuum. The emission line ratios for the cluster members with optical spectra are listed in Table 6 and plotted on the diagnostic diagram of Baldwin et al. (1981, hereafter BPT diagram; see Figure 10).

3.2.3. Star Formation Rates

SFRs based on radio observations are determined for members on the radio–FIR correlation. We include F2, F3 (with notes), F4, F5, and F6. We calculate the star formation rates based on radio luminosity (Yun et al. 2001; Bell 2003; Garn et al. 2009) and compare them to those based on the MIPS 24 μm emission from Rieke et al. (2009), the MIPS 70 μm from Calzetti et al. (2010), and those based on a total infrared luminosity. Equation (6) of Garn et al. (2009), assuming a spectral index of $\alpha = 0.8$, gives the SFRs listed in Table 7. To calculate the SFR from the MIPS 24 μm luminosity, we use Equation (14) of Rieke et al. (2009). We interpolate between bordering redshifts to obtain the proper coefficients $A(z)$ and $B(z)$ from their Table 1. Rates based on total FIR luminosities are calculated from best-fit SEDs to the Polletta et al. (2007) empirical templates and GRASIL population synthesis models (Silk & Rees 1998). We then use the relationship from Kennicutt (1998) for the SFRs. We use these same SED fits to deduce the rest MIPS 70 μm flux from the data in order to be able to use the Calzetti et al. (2010) relationship.

As these galaxies also have optical emission lines, we include the value of the extinction-corrected Hα flux in Table 7. The Hα-derived SFRs included were derived using the formula of

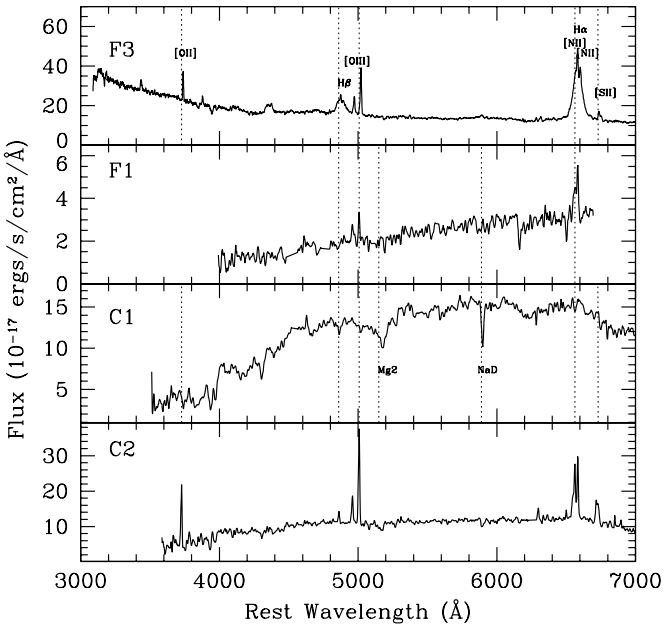

Figure 9. Bright AGNs in the supercluster. AGN Galaxy spectra. From top to bottom: F3 (*ROSAT* point source and known quasar), F1 (double-lobe radio source), C1 (WAT), and C2 (*XMM* point source), as labeled in Figure 1. F3 shows broad emission lines, and C2 shows high [N II] to Hα ratios, typical of AGNs.

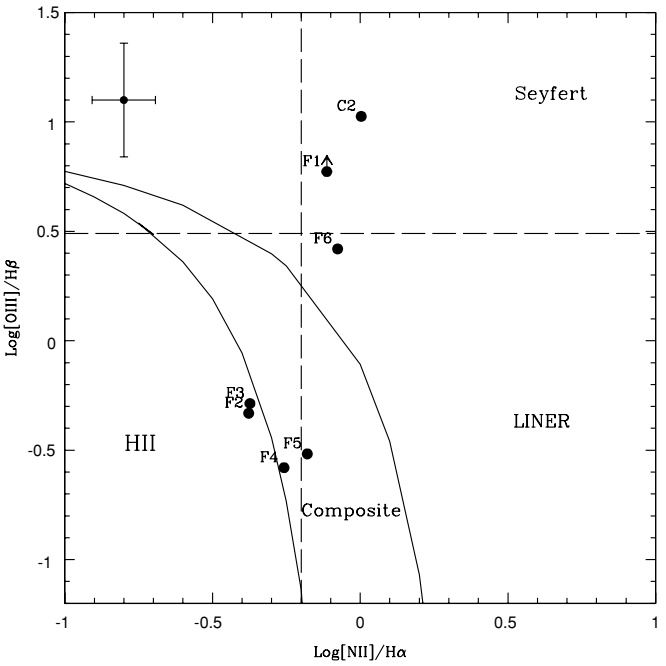

Figure 10. BPT diagram. H II regions, Seyferts, LINERs, and a possible composite of SB and AGN are separated on the BPT diagram. The emission line ratios are listed in Table 6. The sources plotted are those spectroscopically confirmed cluster members with measurable emission lines. Four lie in or near the composite region and two are Seyfert galaxies, and one is on the border of the LINER/Seyfert cut. F3 lies in the composite region but does have broad emission lines characteristic of AGNs. The upper curve is the theoretical separation between SB and AGN from the population synthesis models of Kewley et al. (2001), and the bottom curve is from the observations of Kauffmann et al. (2003). The data point in the top left corner shows error bars based on the average uncertainty in the emission line measurements.

Kennicutt (1998). The Hα derived values tend to be lower than those calculated from the other methods. Whereas the radio and MIPS derived rates are based on observations of about

Table 6
Cluster Member Optical Emission Line Ratios

R.A. (J2000) (deg)	Decl. (J2000) (deg)	log(O III/Hβ)	log(N II/Hα)	z	Notes
203.925201	41.039402	1.0253	0.0033	0.2181	C2
204.152267	41.076385	>0.7731	−0.1130	0.2345	F1
204.179306	41.101704	−0.3310	−0.3774	0.2316	F2
204.480927	41.150002	−0.2867	−0.3731	0.2311	F3, broad lines
204.452316	41.166481	−0.5798	−0.2580	0.2564	F4
204.265793	41.199951	−0.5166	−0.1793	0.2576	F5
204.194122	41.219238	0.4197	−0.0764	0.2330	F6

Table 7
SFRs From Members with Radio and IR Fluxes

$Flux_{Peak}$ (μJy beam^{-1})	$Flux_{24}$ (μJy)	$Flux_{70}$ (mJy)	Flux Hα (10^{-15} cgs)	z_{sp}	$(u'-r')$	SFR_{Rad} ($M_\odot$ yr^{-1})	SFR_{M24} ($M_\odot$ yr^{-1})	SFR_{M70} ($M_\odot$ yr^{-1})	SFR_{SED} ($M_\odot$ yr^{-1})	$SFR_{H\alpha}$ ($M_\odot$ yr^{-1})	Notes
224.4 ± 27.9	12110.8 ± 65.8	56.5 ± 0.8	3.06 ± 0.08	0.2316	1.798	14	94.9	28.9	49.8	3.7	F2
291.6 ± 48.7	4262.4 ± 112.1	...	<140.1	0.2311	0.781	21	27.3	...	60.3	<170.9	F3
419.4 ± 44.3	1899.3 ± 84.2	27.6 ± 0.8	11.03 ± 0.26	0.2564	2.377	35	14.2	14.2	20.0	13.5	F4
277.7 ± 49.9	1799.7 ± 19.2	38.1 ± 0.6	1.42 ± 0.21	0.2576	2.408	136	13.5	22.4	32.8	1.7	F5
219.5 ± 61.4	816.3 ± 17.5	25.5 ± 0.8	2.25 ± 0.09	0.2330	2.535	51	3.9	10.7	15.4	2.7	F6
84	700.2 ± 30.0	...	...	0.2319	2.264	6.4	3.2	...	...	...	88 in A
369	831.7 ± 32.9	...	...	0.2325	2.222	30.5	4.0	...	...	...	96 in B

the same 5″ beam, the Hα fluxes are observed though the smaller 2″ diameter WYIN fibers. Because we do not know the physical extent of the Hα emission, we do not include an aperture correction to the Hα fluxes. We note that if the line emission continues out to the same extent as the beam width of the radio, then a factor of 6.25 could be applied.

The radio-derived rates are usually below but similar to those derived from MIPS, however, F5 and F6 have high values of radio SFRs compared to those from MIPS and optical lines. This is not unlike the difference found between the radio and MIR (based on PAH luminosity) discrepancies found in Sargsyan & Weedman (2009) who studied SFRs in infrared galaxies. Incidents where the radio SFR is significantly higher than the SFRs based on other indicators may be due to contaminating emission from an AGN. F6 has optical emission-line ratios suggesting a possible Seyfert. Also, F3 has broad optical emission lines and is a *ROSAT* X-ray source so likely contaminated by an AGN as well. However, post-SB activity is commonly seen in these types of galaxies (Vanden Berk et al. 2006).

We examined the optical spectra for the few spectroscopically confirmed supercluster galaxies detected in the radio without MIPS detections (Figure 11) to compare the Hα derived SFRs. These are the dark blue points of Figure 1 that are not labeled as either SF or AGN. However, for all cases there is no Hα or Hβ emission, but rather absorption. These galaxies may be regular ellipticals or may reflect their dusty nature where IR and radio observations are important. We are currently preparing a more comprehensive analysis of all the supercluster spectra (D. Fadda et al. 2011, in preparation).

3.3. Bright Radio-excess AGNs in the Field

We observe two member AGNs with radio flux >1.0 mJy beam^{-1}. The first is the BCG at the center of A1763 and the second is F1 which is located along the filament at 13:36:36.2 +41:04:47.3 (J2000), ∼15.3 arcmin from the BCG.

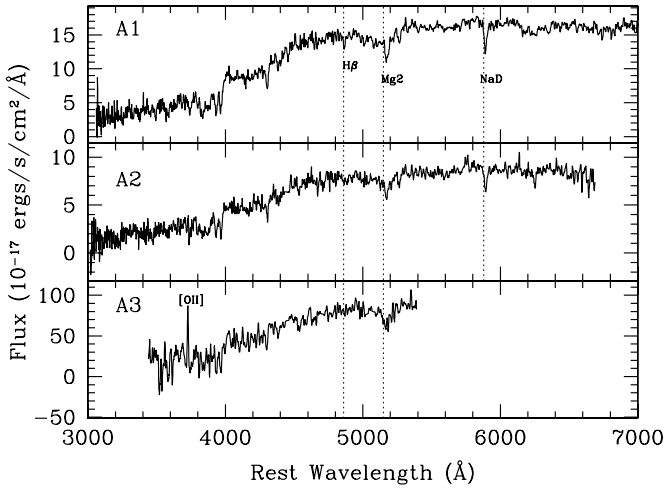

Figure 11. Absorption line galaxies. A1, A2, and A3 (as on Figure 1) all have absorption lines typical of elliptical galaxies.

3.3.1. The WAT BCG at the Center of A1763

The BCG of A1763 is a cD galaxy which is slightly offset from the X-ray peak of 18 arcsec (63 kpc). This galaxy is well documented as a WAT galaxy and radio images have already been published in Owen et al. (1992) and Owen & Ledlow (1997) at the same resolution as our data, as well as in Hardcastle & Sakelliou (2004) at higher resolution and lower frequencies. The radio–FIR fluxes assure us that it is indeed a radio-excess AGN. We include the optical spectrum of this galaxy in Figure 9, which shows a characteristic spectrum of a late-type galaxy, common for cDs. The difference in the optical spectra illustrates the importance of using multiple techniques to identify AGNs in cluster galaxies.

Physical Properties of the WAT. Using the published spectral index of this WAT from Owen & Ledlow (1997) of 1.08, we can calculate several physical properties of the WAT which enable us

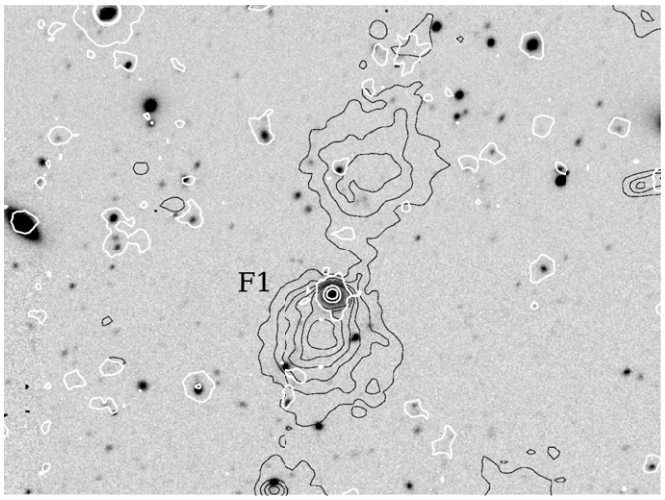

Figure 12. Bright filament AGN. The *R*-band image surrounding the radio-excess galaxy is shown in negative gray scale. The galaxy is located at 13:36:36.2, 41:04:47.3 (J2000) along the filament and NE of the BCG. The thin gray contours show the large symmetric lobes of radio emission and the thick white contours show the MIPS 24 μm emission. This is labeled as F1 in Figures 1 and 9.

to further elucidate the properties of the surrounding intracluster medium (ICM). First, we calculate the total luminosity of the system as in O'Dea & Owen (1987) and assume the full radio spectrum to span from 10 MHz to 100 GHz as in Smolčić et al. (2007). Taking the redshift to be 0.22 which leads to a luminosity distance of 1057 Mpc, we derive $L_{\rm tot} = 6.89 \times 10^{43}$ erg s^{-1}.

Magnetic fields, relativistic particles, and thermal pressure all contribute to the internal pressure in the radio jets (Pacholczyk 1970), and this leads to a method for estimating the contribution of the magnetic fields (Pacholczyk 1970; O'Dea & Owen 1987; Smolčić et al. 2007). Assuming cylindrical symmetry and using the width of the minor axis of the clean beam for the height of the jet (16.6 kpc), as well as a volume filling factor of 1, we assume that the energy of relativistic electrons equals that from relativistic protons and calculate the minimum magnetic field in the southern jet. Here, the flux density is 0.36 Jy beam^{-1}. The value for the magnetic field is 24.4 μG, the minimum energy density is therefore 5.5 $\times$ 10^{-11} dyn cm^{-2}, and the minimum pressure in the jet is therefore 1.8 $\times$ 10^{-11} dyn cm^{-2}.

We can calculate the particle lifetime using the minimum magnetic field calculated above along with the magnetic field of the CMB radiation, which is $4(1 + z)^2$ (O'Dea & Owen 1987). For an electron radiating at 1.4 GHz, the lifetime is $\sim$6 Myr. As the distance between the core and the hotspots in the jets is 20 kpc (Hardcastle & Sakelliou 2004), a jet speed can be estimated of 0.01c. Jet speeds in other WATs have been measured to be 0.04–0.06c (Jetha et al. 2006; Smolčić et al. 2007). Such high speeds are thought to keep the jet resistant to ram pressure as the BCG is near the bottom of the cluster potential well and should not be traveling at high speeds with respect to the ICM.

Hardcastle & Sakelliou (2004), Jetha et al. (2006), and Smolčić et al. (2007) have found that relative speeds as low as 300–500 km s^{-1} are enough to bend WATs embedded in the ICM. From optical spectra of the BCG, and of hundreds of other galaxies in A1763, we have measured the velocity offset of the BCG from the cluster mean. In Paper 0, we published a projected offset of $\sim$260 km s^{-1}. Considering the true velocity could be higher depending on the true direction of motion, this velocity is consistent with those calculated in the hydrodynamic models.

3.3.2. A Bent Double-lobe Radio Galaxy along the Supercluster Filament

Figure 12 shows the *R*-band image of F1 with radio and 24 μm contours overlaid. This source is well below both the 24 μm and 70 μm radio–FIR correlations. We note that this source is classified as an AGN whether or not the flux from the lobes is included. Figure 9 shows the corresponding optical spectrum (F1, also discussed in Paper 0). High [N II] emission relative to Hα is seen, a characteristic of AGN or LINER activity. The bright radio core of this double lobe source appears to be at the edge of the brighter lobe, and the fainter lobe is more extended, implying that we may be viewing a bent double-lobe source on an angle. A full discussion of this source, its likely bent morphology, and its implications for the surrounding intra-filament medium are detailed in a separate work (Edwards et al. 2010b).

4. DISCUSSION

4.1. The AGNs and Starburst Fractions

The majority of bright FIR cluster sources are SB systems. We have determined this using the radio–FIR correlation, the IRAC color diagnostic and through matching to X-ray point source and known quasar catalogs. However, for the few sources that have bright MIPS and bright radio emission as well, the fraction of AGN sources rises highly to nearly 50%. This is consistent with the results of Smolčić et al. (2008) who find roughly 50% of sub-mJy radio sources in the COSMOS field at redshifts between 0.2 and 0.3 are AGNs and roughly half are SBs.

4.1.1. Radio Galaxies with MIPS 24 μm < 4 mJy are SB

We already found at the average of our stacked low-radio flux MIPS 24 μm selected sample was described by SB activity. But are we missing a large population of AGNs with FIR emission below our MIPS 24 μm sensitivity? To estimate the number of AGNs we may be missing, we study the radio luminosity function, particularly that of cluster galaxies. Yun et al. (2001) construct a radio luminosity function of infrared-selected galaxies out to a redshift of 1.5. They find that SBs and AGNs show a bimodal distribution, with AGNs having 1.4 GHz luminosities over 10^{23} W Hz^{-1} and SBs having lower radio luminosities. By studying over 2000 SDSS galaxies, Best et al. (2005) also find that the SB galaxies dominate over the AGN population below 1.4 GHz luminosities of 10^{23} W Hz^{-1}. However, the cluster AGN number density is much higher than in the field (Lin & Mohr 2007), so it would be prudent to look at radio luminosity functions built on cluster galaxies. Miller & Owen (2002) constructed a radio luminosity function based on galaxies in nearby galaxy clusters, also finding that star formation dominates in galaxies with radio luminosities less than 5 $\times$ 10^{22} W Hz^{-1}. According to this, the galaxies below our detection limits (10^{22} W Hz^{-1}) should be star forming.

However, recent work by Miller et al. (2009) on the Coma cluster has found some surprising results. Though the authors give the caveat of a possible selection bias, they find fewer numbers of star-forming galaxies than AGNs at very low radio luminosities. By constructing a very deep radio luminosity function, the authors indeed find that low luminosity radio sources ($\sim$log $L_{1.4\,\rm GHz} = 22.2$) are dominated by star-forming systems, but at the very low radio luminosities ($\sim$log $L_{1.4\,\rm GHz}$<21), the AGN

Table 8
Number of Active Galaxies

Number of Radio Galaxies	Filament	Area (deg^2)	Density (deg^{-2})	Outside	Area (deg^2)	Density (deg^{-2})
	230	0.36	639	361	0.54	669
+ z_{sp}	11	0.36	33	1	0.54*	2
+ MIPS	33	0.20	165	44	0.26	169
+ MIPS+ z_{sp}	8	0.20	45	0	0.26*	0
+ MIPS SF	18	0.20	90	4	0.26	7
+ MIPS SF+ z_{sp}	5	0.20	35	0	0.26*	0
+ MIPS AGN	22	0.20	110	37	0.26	69
+ MIPS AGN+ z_{sp}	3	0.20	15	0	0.26*	0

contribution to the radio luminosity function again becomes important. Such low luminosities are below our radio detection limits, so if A1763 has a similar radio luminosity function to Coma, we may in fact be missing some low-luminosity AGNs. For sources at the redshift of A1763, log $L_{1.4\,GHz} \sim 21$, corresponds to a radio flux of 9.6 μJy—much below our radio detection limit. Following the FIR–radio correlation, and assuming it is valid at these lower luminosities, the corresponding MIPS 24 μm flux for an AGN would have to be 96 μJy or below. Such a value is just below the 3σ depth of 120 μJy for our MIPS observations, so it is possible that our observations could include some of these galaxies, but they should not form a large population of the MIPS-selected cluster galaxies. In fact, there are 133 (out of 10,876) MIPS sources with 24 μm flux less than 100 μJy, but only two are spectroscopically confirmed cluster members.

4.2. Activity as a Function of Environment

Table 8 lists the number and number density of active galaxies in the filament with radio detections (which includes the area of both clusters and a cylinder the width of approximately the virial radius of A1763, gray circles from Figure 1). The number density of radio and radio+MIPS-detected galaxies inside and outside of the filament is approximately the same, 165 and 169 deg^{-2}, respectively. However, when looking at only the superstructure members, there is a higher number density of active galaxies inside the filament than in the outskirts and field (MIPS SF and MIPS AGN in Table 8). In fact, this region is dominated by the SB candidates and not the radio-excess AGN as the number density for star-forming galaxies in the filament is higher than in the outskirts, whereas the number of AGNs is higher in the outskirts. This shows that the filament is more active than the local field and outskirts and that it is not the radio-excess AGN that dominates the activity. It is remarkable that 9 of 11 of the quasars at the cluster redshift are found on the outskirts of the superstructure.

4.3. Cluster Scale Morphology and the Double-lobe Radio Sources

The current study provides three additional pieces of evidence which add to our claims of an ongoing merger or large-scale flow of cluster-feeding galaxies made in Paper 0.

First, the *XMM* image reveals that the ICM is elongated along a southwest–northeast direction (Figure 13), with a cooler long tail of gas toward the southwest, similar to the case of A85 (Durret et al. 2003). There is also a small displacement between the projected position of the BCG and the peak of X-ray emission. This suggests that some kind of merging or flow has taken place along this direction.

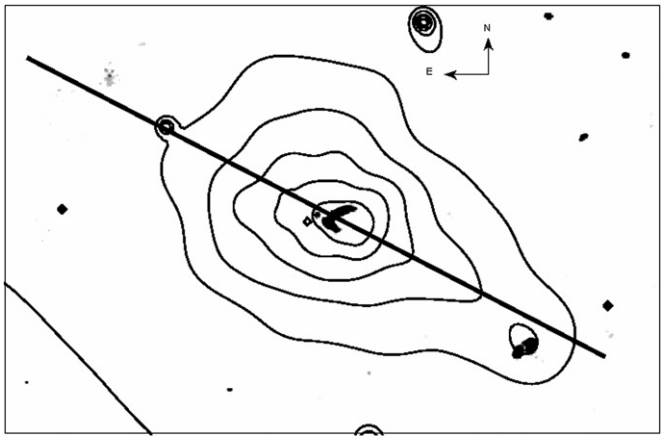

Figure 13. BCG of A1763. A ~16 arcmin ×10 arcmin field centered on the BCG of A1763. This is a cD galaxy in the optical and appears as a bright WAT in the 1.4 GHz images. The background image is the 1.4GHz data. This schematic shows X-ray contours from *XMM* overlaid. The X-ray emission is elongated in the same direction as the cluster-feeding filament, and as the WAT tails. The black line shows the direction toward the cluster-feeding filament galaxies and is angled at 25° N of E.

Second, the A1763 WAT consists of two tails, angled *away* from the direction of the cluster filament. This can be seen in Figure 13 where we overplot the X-ray contours on our 1.4 GHz image. Note that the WAT is offset from the X-ray brightness peak by ~100 kpc (first noted in Paper 0). The two jets are oriented perpendicular to the large-scale morphology of the cluster X-ray emission, which itself has a projected elongation in the same direction as the cluster filament. The two large radio plumes have similar brightnesses, a ratio of 1.15 (Hardcastle & Sakelliou 2004), though the brightness ratio of the jets has been reported by Jetha et al. (2006) to be much higher at 4.7. The plumes bend with the X-ray morphology and are parallel with the line of the cluster-feeding filament galaxies. These data are consistent with the suggestion in Douglass et al. (2008), that the WAT morphology is an example of cool gas from the structure of the filament raining onto the cluster potential, at the location of the BCG. We take this as further evidence for the existence of the cluster-feeding filament. In a future article, we will include a discussion of the velocity dispersions and cluster components found from the analysis of the cluster galaxies optical spectra. Bent double-lobe radio sources are rare, and that we have a second one in the same large-scale structure may allude to the dynamics in the system.

Finally, a score of lower luminosity quasars are found at the outskirts of the high galaxy density regions of the supercluster, with no quasars inside the cluster cores. This type of behavior in low luminosity quasars has previously been associated with merging clusters (Söchting et al. 2002, 2004), at least for redshifts below $z \sim 0.3$.

5. SUMMARY AND CONCLUSIONS

We have examined 1.4 GHz radio sources in the supercluster of A1763–A1770. We investigate the radio–FIR correlation, the location of X-ray point sources, the IRAC colors, and the location of known quasars to look at the frequency of occurrence of AGNs in the sample of MIPS and radio-selected galaxies. Taking advantage of radio upper limits derived from our data and MIPS fluxes from Paper I, we conclude that the MIPS cluster galaxies that lie in the filament are mostly SBs and not AGNs. We measure q_{24} for eight radio-bright member galaxies. Five are classified SB galaxies, all along the filament. One AGN is located along the filament, and the other two AGNs are inside the core of A1763. For the galaxies classified as radio SB, we calculate the radio SFRs and compare to those from the FIR and Hα measurements. More redshifts of the radio galaxies would help increase our ability to discriminate between SB versus AGN inside and outside the superstructure.

We calculate physical properties of the central WAT and of F1 and relate them to the large-scale structure of this system mapped by *XMM*. The BCG velocity is consistent with those induced in cluster–sub-cluster mergers and the morphology of the WAT and its orientation away from the cluster-feeding filament suggests a relationship with the large-scale flow of the cluster-feeding filament and its ICM (Loken et al. 1995; Gomez et al. 1997). F1 is the first bent DLRS to be identified within a known supercluster filament. We suggest clusters which host a central WAT and/or a source like F1 near to galaxy clusters may be good tracers for superclusters scale filaments.

There exist a number of quasars with redshifts consistent with those of the superstructure, at those on the outskirts of the system, a phenomenon previously associated with merging systems. Another method of selecting galaxy clusters with large filaments such as these would be to focus on superclusters near quasar triplets, which are rare. Deeper X-ray observations would help elucidate the large-scale cluster dynamics.

If Coma, our closest rich cluster, is similar to other systems further out, it would be prudent for us to extend this study to even lower radio luminosities in order to fully uncover the contaminating AGN population to our study of SB in the A1763 filament. Although, our *Spitzer* observations are likely not deep enough to find significant numbers of this radio-faint AGN population. The improved sensitivity of the EVLA and Herschel will make these types of studies possible.

We thank the scientific staff at the NRAO, in particular G. Van Moorsel for help with observation planning and F. Owen for help with data reduction techniques. We thank A. Biviano for his reading and comments on this manuscript and for constructing the FIR SEDs. We also thank the anonymous referee for extremely helpful comments that contributed to a much improved version of this paper.

Support for this work was provided by NASA through an award issued by JPL/Caltech. This work is based in part on original observations using the Very Large Array operated by the NRAO. The National Radio Astronomy Observatory is a facility of the National Science Foundation operated under cooperative agreement by Associated Universities, Inc. This work is also based in part on archival observations obtained with *XMM-Newton*, an ESA science mission with instruments and contributions directly funded by ESA Member States and NASA and observations made with *Spitzer*, a space telescope operated by the Jet Propulsion Laboratory, California Institute of Technology, under a contract with NASA. Funding for the SDSS and SDSS-II has been provided by the Alfred P. Sloan Foundation, then Participating Institutions, the National Science Foundation, the US Department of Energy, NASA, the Japanese Monbukagakusho, the Max Planck Society, and the Higher Education Funding Council of England. The SDSS is managed by the Astrophysical Research Consortium for the Participating Institutions (see list at http://www.sdss.org/collaboration/credits.html). We have made use of the *ROSAT* Data Archive of the Max-Planck-Institut für extraterrestrische Physik (MPE) at Garching, Germany as well as the *XMM-Newton* Data Archive.

Facilities: Spitzer (IRAC, MIPS), VLA, XMM, WIYN (Hydra)

REFERENCES

Appleton, P. N., et al. 2004, ApJS, 154, 147
Baldwin, J. A., Phillips, M. M., & Terlevich, R. 1981, PASP, 93, 5
Bell, E. F. 2003, ApJ, 586, 794
Best, P. N., Kauffmann, G., Heckman, T. M., Brinchmann, J., Charlot, S., Ivezić, Ž., & White, S. D. M. 2005, MNRAS, 362, 25
Bond, J. R., Kofman, L., & Pogosyan, D. 1996, Nature, 380, 603
Burns, J. O., Gregory, S. A., & Holman, G. D. 1981, ApJ, 250, 450
Calzetti, D., et al. 2010, ApJ, 714, 1256
Carter, J. A., & Read, A. M. 2007, A&A, 464, 1155
Ciliegi, P., Zamorani, G., Hasinger, G., Lehmann, I., Szokoly, G., & Wilson, G. 2003, A&A, 398, 901
Clowe, D., Bradač, M., Gonzalez, A. H., Markevitch, M., Randall, S. W., Jones, C., & Zaritsky, D. 2006, ApJ, 648, L109
Condon, J. J. 1992, ARA&A, 30, 575
Condon, J. J. 1997, PASP, 109, 166
Coziol, R., Andernach, H., Caretta, C. A., Alamo-Martínez, K. A., & Tago, E. 2009, AJ, 137, 4795
De Lucia, G., & Blaizot, J. 2007, MNRAS, 375, 2
Donley, J. L., Rieke, G. H., Pérez-González, P. G., & Barro, G. 2008, ApJ, 687, 111
Douglass, E. M., Blanton, E. L., Clarke, T. E., Sarazin, C. L., & Wise, M. 2008, ApJ, 673, 763
Durret, F., Lima Neto, G. B., Forman, W., & Churazov, E. 2003, A&A, 403, L29
Edwards, L. O. V., Fadda, D., Biviano, A., & Marleau, F. R. 2010a, AJ, 139, 434
Edwards, L. O. V., et al. 2010b, submitted
Eisenhardt, P. R., et al. 2004, ApJS, 154, 48
Fadda, D., Biviano, A., Marleau, F. R., Storrie-Lombardi, L. J., & Durret, F. 2008, ApJ, 672, L9
Finn, R. A., Balogh, M. L., Zaritsky, D., Miller, C. J., & Nichol, R. C. 2008, ApJ, 679, 279
Garn, T., Green, D. A., Riley, J. M., & Alexander, P. 2009, MNRAS, 397, 1101
Gomez, P. L., Ledlow, M. J., Burns, J. O., Pinkey, J., & Hill, J. M. 1997, AJ, 114, 1711
Gonzalez, R. E., & Padilla, N. E. 2009, MNRAS, 397, 1498
Griffith, R. L., & Stern, D. 2010, AJ, 140, 533
Hardcastle, M. J., & Sakelliou, I. 2004, MNRAS, 349, 560
Helou, G., Soifer, B. T., & Rowan-Robinson, M. 1985, ApJ, 298, L7
Hickox, R. C., et al. 2009, ApJ, 696, 891
Imanishi, M., Dudley, C. C., Maiolino, R., Maloney, P. R., Nakagawa, T., & Risaliti, G. 2007, ApJS, 171, 72
Jetha, N. N., Hardcastle, M. J., & Sakelliou, I. 2006, MNRAS, 368, 609
Jones, C., & Forman, W. 1984, ApJ, 276, 38
Kauffmann, G., Colberg, J. M., Diaferio, A., & White, S. D. M. 1999, MNRAS, 307, 529
Kauffmann, G., et al. 2003, MNRAS, 346, 1055
Kennicutt, R. C., Jr. 1998, ARA&A, 36, 189
Kewley, L. J., & Dopita, M. A. 2002, ApJS, 142, 35
Kewley, L. J., Dopita, M. A., Sutherland, R. S., Heisler, C. A., & Trevena, J. 2001, ApJ, 556, 121
Lacy, M., Storrie-Lombardi, L. J., & Sajina, A., e. a. 2004, ApJS, 154, 166
Laganá, T. F., Lima Neto, G. B., Andrade-Santos, F., & Cypriano, E. S. 2008, A&A, 485, 633
Lin, Y.-T., & Mohr, J. J. 2007, ApJS, 170, 71
Loken, C., Roettiger, K., Burns, J. O., & Norman, M. 1995, ApJ, 445, 80
Marleau, F. R., Fadda, D., Appleton, P. N., Noriega-Crespo, A., Im, M., & Clancy, D. 2007, ApJ, 663, 218

Miley, G. K., Perola, G. C., van der Kruit, P. C., & van der Laan, H. 1972, Nature, 237, 269
Miller, C. J., Nichol, R. C., & Reichart, e. a. 2005, AJ, 130, 968
Miller, N. A., Hornschemeier, A. E., Mobasher, B., Bridges, T. J., Hudson, M. J., Marzke, R. O., & Smith, R. J. 2009, AJ, 137, 4450
Miller, N. A., & Owen, F. N. 2002, AJ, 124, 2453
Navarro, J. F., Frenk, C. S., & White, S. D. M. 1995, MNRAS, 275, 56
O'Dea, C. P., & Owen, F. N. 1987, ApJ, 316, 95
Owen, F. N., & Ledlow, M. J. 1997, ApJS, 108, 41
Owen, F. N., Ledlow, M. J., & Keel, W. C. 1995, AJ, 109, 14
Owen, F. N., & Morrison, G. E. 2008, AJ, 136, 1889
Owen, F. N., & Rudnick, L. 1976, ApJ, 205, L1
Owen, F. N., White, R. A., & Burns, J. O. 1992, ApJS, 80, 501
Pacholczyk, A. G. 1970, Radio Astrophysics: Nonthermal Processes in Galactic and Extragalactic Sources (San Francisco, CA: Freeman)
Peres, C. B., Fabian, A. C., Edge, A. C., Allen, S. W., Johnstone, R. M., & White, D. A. 1998, MNRAS, 298, 416
Polletta, M., et al. 2007, ApJ, 663, 81
Rieke, G. H., Alonso-Herrero, A., Weiner, B. J., Pérez-González, P. G., Blaylock, M., Donley, J. L., & Marcillac, D. 2009, ApJ, 692, 556
Sajina, A., Lacy, M., & Scott, D. 2005, ApJ, 621, 256
Sakelliou, I., & Merrifield, M. R. 2000, MNRAS, 311, 649
Sargsyan, L. A., & Weedman, D. W. 2009, ApJ, 701, 1398
Silk, J., & Rees, M. J. 1998, A&A, 331, 1
Smolčić, V., Schinnerer, E., & Scodeggio, e. a. 2008, ApJS, 177, 14
Smolčić, V., et al. 2007, ApJS, 172, 295
Söchting, I. K., Clowes, R. G., & Campusano, L. E. 2002, MNRAS, 331, 569
Söchting, I. K., Clowes, R. G., & Campusano, L. E. 2004, MNRAS, 347, 1241
Springel, V., et al. 2005, Nature, 435, 629
Sutherland, W., & Saunders, W. 1992, MNRAS, 259, 413
Umetsu, K., Medezinski, E., Broadhurst, T., Zitrin, A., Okabe, N., Hsieh, B.-C., & Molnar, S. M. 2010, ApJ, 714, 1470
Vanden Berk, D. E., et al. 2006, AJ, 131, 84
Véron-Cetty, M., & Véron, P. 2006, A&A, 455, 773
Vikhlinin, A., Markevitch, M., Murray, S. S., Jones, C., Forman, W., & Van Speybroeck, L. 2005, ApJ, 628, 655
White, D. A. 2000, MNRAS, 312, 663
Yun, M. S., Reddy, N. A., & Condon, J. J. 2001, ApJ, 554, 803
Zhang, Y.-Y., Reiprich, T. H., Finoguenov, A., Hudson, D. S., & Sarazin, C. L. 2009, ApJ, 699, 1178